AMERICAN SOCIETY FOR MICROBIOLOGY | Journal of Bacteriology®

RESEARCH ARTICLE

Double Tubular Contractile Structure of the Type VI Secretion System Displays Striking Flexibility and Elasticity

Maria Silvina Stietz,[a,b,c] Xiaoye Liang,[a,b,c] Megan Wong,[a,b,c] Steven Hersch,[a,b,c] Tao G. Dong[a,b,c]

[a]Ecosystem and Public Health, Faculty of Veterinary Medicine, University of Calgary, Calgary, Alberta, Canada
[b]Snyder Institute for Chronic Diseases, University of Calgary, Calgary, Alberta, Canada
[c]Biochemistry and Molecular Biology, Cumming School of Medicine, University of Calgary, Calgary, Alberta, Canada

ABSTRACT Antimicrobial treatment can induce many bacterial pathogens to enter a cell wall-deficient state that contributes to persistent infections. The effect of this physiological state on the assembly of transenvelope-anchored organelles is not well understood. The type VI secretion system (T6SS) is a widespread molecular weapon for interspecies interactions and virulence, comprising a long double tubular structure and a transenvelope/baseplate complex. Here, we report that cell wall-deficient spheroplasts assembled highly flexible and elastic T6SS structures forming U, O, or S shapes. Upon contacting the inner membrane, the T6SS tubes did not contract but rather continued to grow along the membrane. Such deformation likely results from continual addition of sheath/tube subunits at the distal end. Induction of TagA repressed curved sheath formation. Curved sheaths could also contract and deliver T6SS substrates and were readily disassembled by the ClpV ATPase after contraction. Our data highlight the dramatic effect of cell wall deficiency on the shape of the T6SS structures and reveal the elastic nature of this double tubular contractile injection nanomachine.

IMPORTANCE The cell wall is a physical scaffold that all transenvelope complexes have to cross for assembly. However, the cell wall-deficient state has been described as a common condition found in both Gram-negative and Gram-positive pathogens during persistent infections. Loss of cell wall is known to have pleiotropic physiological effects, but how membrane-anchored large cellular organelles adapt to this unique state is less completely understood. Our study examined the assembly of the T6SS in cell wall-deficient spheroplast cells. We report the elastic nature of contractile T6SS tubules under such conditions, providing key insights for understanding how large intracellular structures such as the T6SS accommodate the multifaceted changes in cell wall-deficient cells.

KEYWORDS type VI secretion system, bacteriophage, spheroplast, elastic rod, elasticity, contractile tubes, L-form, T6SS, cell wall, sheath

Bacteria have evolved with various mechanisms to protect themselves and outcompete neighboring species in complex communities (1). The antagonistic interactions mediated by the activities of those bacterial weapons can dictate community structures and dynamic changes (2–4). The type VI secretion system (T6SS) is one such lethal weapon used by many Gram-negative bacteria to deliver toxic effectors into neighboring bacterial and eukaryotic cells (5–7). Encoded by 13 conserved genes, the T6SS structure consists of a membrane complex (TssJLM), a baseplate (TssK-TssEFG), and a double tubular structure comprising an outer VipA/B (TssB/C) sheath encircling an inner needle-like Hcp tube (8–14). At the tip of the tube sits a spike complex, VgrG/PAAR, that not only sharpens the tube but also serves as a main loading site for effectors (15–18). The inner tube and the outer sheath share the same six-start helical

Citation Stietz MS, Liang X, Wong M, Hersch S, Dong TG. 2020. Double tubular contractile structure of the type VI secretion system displays striking flexibility and elasticity. J Bacteriol 202:e00425-19. https://doi.org/10.1128/JB.00425-19.

Editor Victor J. DiRita, Michigan State University

Address correspondence to Tao G. Dong, tdong@ucalgary.ca.

Received 21 June 2019
Accepted 14 October 2019
Accepted manuscript posted online 21 October 2019
Published 6 December 2019

structures, with each ring composed of hexamers of Hcp and heterodimeric VipA/B, respectively (12, 13). The T6SS structure assembles from the baseplate and polymerizes inward with new subunits added to the distal end, often spanning the cell (9). The distal end is capped by TssA, which was previously shown to play a key role in baseplate assembly and recruitment of sheath/tube precursors (19–21). A recent report found that TagA, a distant paralog of TssA, interacts with TssA and stops sheath/tube extension in enteroaggregative *Escherichia coli* (21). The extended sheath is in a high-energy conformation, and its contraction was previously proposed to initiate from the baseplate side and continue to the distal end, shortening the sheath by half within 2 ms (9, 22). After contraction, the N terminus of VipB is exposed and recognized by the AAA^+ (ATPase associated with various cellular activities positive) ATPase ClpV (23–26), which disassembles the contracted sheath and enables recycling of sheath subunits for another assembly. Unlike the sheath that remains inside, the inner Hcp tube is ejected after contraction and requires *de novo* synthesis for replenishment and is hence under transcriptional regulation different from that controlling the sheath subunits (27).

Although the cell wall confers crucial protection to bacteria, cell wall-deficient cells, including L-form cells, could be selected for under certain clinical conditions and have been shown to be associated with a number of infectious diseases, including persistent infections in urinary and respiratory systems (28–30). Disruption of the cell wall is known to cause pleiotropic physiological effects, including excess lipid synthesis and oxidative stress (31, 32). In contrast, how the loss of cell wall-mediated physical constraint affects the assembly of intracelluar organelles is not well understood. Basler and coworkers previously demonstrated that spheroplast *Vibrio cholerae* cells could assemble long and functional T6SS tubules proportional to the enlarged cell size, indicating that the cell wall is not required for supporting the T6SS transenvelope anchor (9). In this study, we investigated how excess membrane synthesis of spheroplast cells affects T6SS assembly. As the T6SS tail polymerizes from its membrane anchor toward the opposite side of the cytoplasmic membrane, irregular membrane vesicles formed in spheroplasts might directly interfere with T6SS polymerization by blocking extension and triggering contraction. Here, we report that, to our surprise, the cytoplasmic membrane of spheroplasts guided the extension of the growing T6SS sheath upon contact such that the T6SS structures adopted different degrees of curved deformation ranging from hook-like to circular shapes. Curved sheath structures were straightened after contraction or removal of the membranes by detergents, suggesting that membrane contact physically dictates the sheath shape. Expression of TagA inhibited the formation of curved structures, while deletion of *tagA* resulted in curved structures in *V. cholerae* rod cells. Although the average stalling time between sheath polymerization termination and contraction was reduced by *tagA* deletion in both rod and spheroplast cells, a considerable number of sheaths exhibited stalling in the *tagA* mutant, indicating that the extended sheath could maintain temporary stability independently of TagA. The curved sheaths were capable of contraction and delivery of Hcp and VgrG and were subject to disassembly by ClpV. Noncontractile curved sheaths were straightened after membrane lysis. Our data not only demonstrate the flexibility and elasticity of the double tubular T6SS but also highlight the multifaceted effect of losing an intact cell wall on intracellular structures.

RESULTS

Membrane-guided continual extension of the double tubular structures upon contact. To induce spheroplast cells with excess membrane synthesis (31, 33), we treated *V. cholerae* with ampicillin as previously described (9) but imaged the cells after subjecting them to longer exposure to the antibiotic. As expected, many *V. cholerae* spheroplasts formed visible internal vesicles under this condition (Fig. 1A). Surprisingly, we observed highly curved T6SS structures instead of the membrane-triggered early termination that we had initially postulated (Fig. 1A and B) (see Fig. S1A and Movie S1 in the supplemental material). Upon contact, the membrane did not trigger contraction but rather guided a polymerizing straight sheath to bend along its length and continue

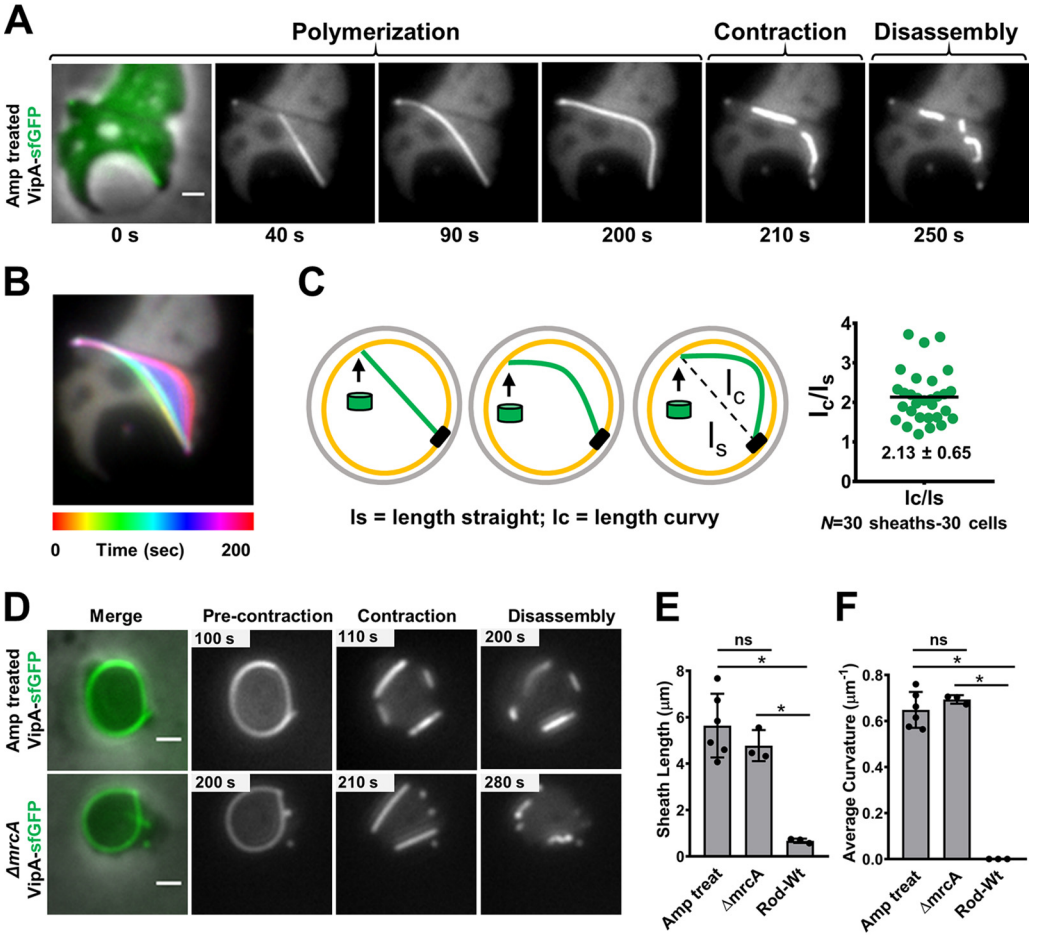

FIG 1 Curved sheath polymerization guided by membrane contact. (A) Sheath assembly in the VipA-sfGFP-labeled strain treated with ampicillin. The image at the left is of a merge of the phase and GFP (green) channels. The images in the series correspond to 5-min time-lapse videos (10 s per frame). Scale bar, 1 μm. Additional examples can be found in Fig. S1A and Movie S1 in the supplemental material. (B) Temporal color-coded image corresponding to sheath polymerization (0 to 200 s) of the cell depicted in panel A. The color code (spectrum) and time scale are shown at the bottom of the panel. (C) Model of initially straight sheath (green) followed by curved polymerization. Green cylinders represent sheath subunits. The scatterplot on the right shows the ratio of the initial straight length of the sheath (l_S) over the total curvy length of the sheath (l_C), measured for 30 sheaths. (D) Images show precontraction and contraction and disassembly of curved sheaths formed by the VipA-sfGFP-labeled ampicillin (Amp)-treated cells (top panel) and *mrcA* deletion cells (bottom panel). The panels at the left represent merges of the phase and green (GFP) channels. All images are representative examples of results from at least three biological replicates. Scale bars, 1 μm. (E and F) Sheath length (E) and average curvature (calculated using Kappa) (F) of sheaths formed in ampicillin-treated ($n = 80$) and *mrcA* deletion ($n = 40$) spheroplasts and rod cells ($n = 150$). Each data point represents an independent biological replicate. Graphs show mean values (bars) ± SD (lines). ns, nonsignificant; *, $P < 0.05$ (unpaired t test); Wt, wild type.

to extend. After the sheath's distal end contacted the membrane, we observed an arching deformation, suggesting that there is continual addition of VipA/B and Hcp precursors to the growing structure (Fig. 1B and C). The curved sheaths can still increase their length by 2-fold on average in comparison with the initial straight length or the linear distance from the baseplate to the distal end (Fig. 1C).

To rule out the possibility that the curved extended sheaths are a result of some unknown properties of ampicillin other than targeting cell wall synthesis, we examined T6SS formation in the deletion mutant of *mrcA*, encoding the cell wall synthesis enzyme PBP1a, whose absence is known to disrupt the cell wall and to cause a spherical shape to form in *V. cholerae* (34, 35). We found that long and curved T6SS sheaths were similarly formed in both the ampicillin-treated cells and the *mrcA* mutant cells, widely exciding the sheath length in rod cells (Fig. 1D and E) (see Fig. S1B in the supplemental material). Among the 120 curved sheaths that we measured, the average curvature of

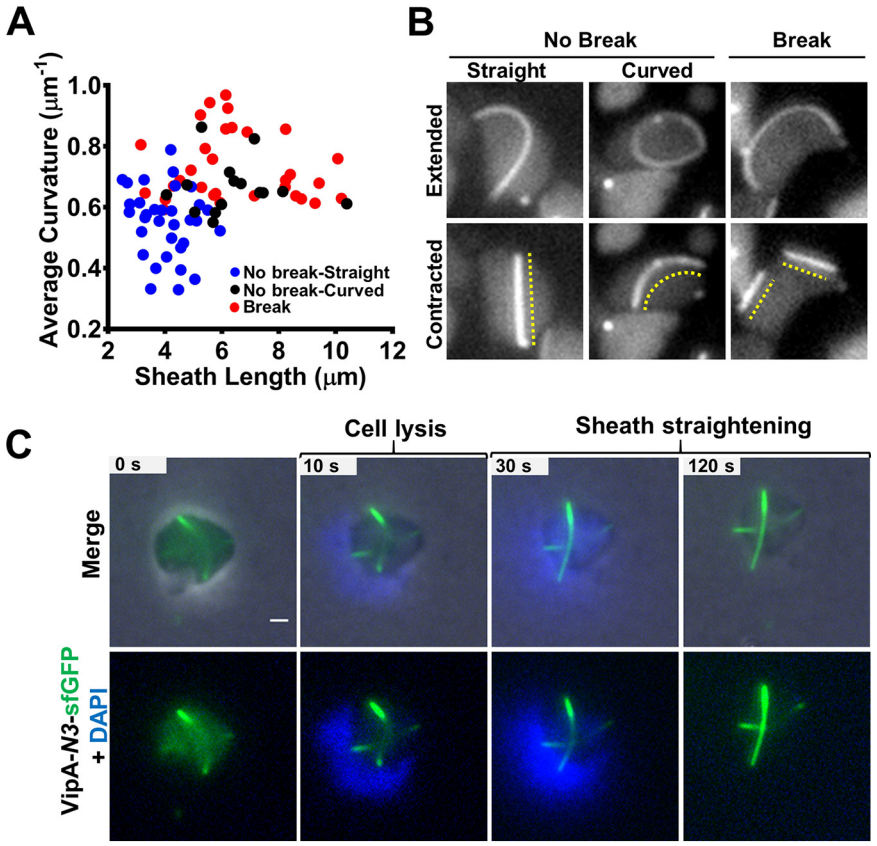

FIG 2 Straightening of T6SS sheath upon contraction and cell lysis. (A) Scatterplot showing the dispersion of the extended sheath length and the average curvature of contraction types in ampicillin-treated cells as follows: normal contraction, straightened (No break-Straight; $n = 33$); normal contraction, slightly curved (No break-Curved; $n = 15$); and sheaths that break into pieces after contraction (Break; $n = 31$). Each data point represents a sheath. (B) Sheaths formed in ampicillin-treated cells that contract normally (No Break) and straighten after contraction (left) or remain slightly curved (middle) and those that break (Break) into pieces after contraction (right). The dashed lines indicate the contracted sheath. Images were taken from a 5-min time-lapse video (10 s per frame). (C) Noncontractile VipA-N3–sfGFP curved sheath straightening after cell lysis induced by 80 μg/ml colistin–0.1% Triton X-100. Nucleic acid was stained with 10 μg/ml DAPI. Top row, merge of phase, GFP (green), and DAPI (blue) channels. Bottom row, green and blue channels only. The original video was an 8-min time-lapse video (10 s per frame). Scale bar, 1 μm. The full video is included in Movie S3 in the supplemental material (cell1). An additional example is provided in Fig. S3B in the supplemental material.

the extended sheaths formed in ampicillin-treated cells (0.64 μm^{-1}, $n = 80$) was comparable to that in the *mrcA* mutant (0.69 μm^{-1}, $n = 40$), while no deformation was observed in 150 sheaths formed in rod cells (Fig. 1F) (see Fig. S1B in the supplemental material). When we measured the curvature at each point along individual sheaths, the maximum curvature points reached up to 2.3 μm^{-1} (mean, 1.22 μm^{-1}; $n = 120$) (see Fig. S1C and D in the supplemental material). These results demonstrate the remarkable flexibility of the T6SS double tubular extending sheath/Hcp structure, previously described as a rigid structure (36, 37), and suggest that membrane contact is not a sufficient trigger for contraction.

Abolishing membrane constraint straightens curved structures. Contraction of the curved sheaths generally straightens the structures, likely due to loss of membrane contact at one or both ends (Fig. 1D) (see Fig. S1C in the supplemental material). Contraction could also break the sheath structures into pieces, which is more likely to occur for longer and more extensively curved structures (Fig. 2A) (see Fig. S2A in the supplemental material). Although the spheroplasts exhibited a wide range of cell sizes (see Fig. S2B in the supplemental material), the break or no-break outcome of the sheath contraction correlated with the sheath curvature but not with cellular size (see

Fig. S2C in the supplemental material). A small number of contracted sheaths remained slightly curved after contraction (Fig. 2B), and they were significantly longer than the straight contracted sheaths (see Fig. S2D in the supplemental material), suggesting that they had maintained membrane contact. In addition, the contracted and break-free sheath pieces were similarly disassembled, suggesting that the disassembly process does not require attachment to baseplate (Fig. 1D). These results indicate that membrane contact is required to confine the elastic double tubules into the curvy form.

Next, we investigated whether the curved extended structures were elastic rather than fixed into a permanent shape. We postulated that removal of membrane constraint would straighten the sheaths. To test this and avoid the complexity of contraction, we used the *vipA-N3* mutant, in which the sheath-Hcp tube is locked into the extended form (38). The noncontractile extended sheath was able to assemble curved structures similar to those seen with the wild type, while no contraction was observed (see Fig. S3A and Movie S2 in the supplemental material). When cells were treated with Triton X-100 and colistin to induce lysis, the curved structures straightened after escaping from the cells (Fig. 2C) (see Fig. S3B and Movie S3 in the supplemental material), indicating that the extended double tubule structures were indeed elastic.

Formation of curved T6SS structure is reduced by TagA induction. We then investigated why curved structures are formed in spheroplast cells. Because the curved structure likely results from continual addition of precursors at the growing end of the sheath/tube upon contact with the membrane, we postulated that TagA, the sheath-extension stopper (21), may be involved in determining the curved shape in spheroplast cells. Induction of *tagA* substantially reduced curved structure formation (Fig. 3A and B and C) (see Movie S4 in the supplemental material). Deletion of *tagA* showed curved structures in rod cells but did not affect killing ability (see Fig. S4A and B in the supplemental material). Notably, the average measurements of curvature of sheaths observed in the *tagA* mutant in rods (0.74 μm^{-1}) and spheroplast cells (0.69 μm^{-1}) were comparable to that of wild-type spheroplasts (0.64 μm^{-1}) (Fig. 3D).

TagA is not required for entering the stalling stage between extension and contraction. Consistent with the previous observation in *E. coli* (21), we also found that there is a stalling stage (~50 s [median value]) during which the extended sheath is maintained in unchanged form in both rod and spheroplast cells (Fig. 3E) (see Fig. S4C in the supplemental material). Although the stalling stage/residence time is shorter in both the *tagA* rod cells (~25 s [median value]) and the ampicillin-treated *tagA* spheroplasts (~30 s [median value]) of *V. cholerae*, a large number of sheath structures remained stable in the extended form in the *tagA* mutant (Fig. 3E). Among the stalled structures in *tagA*, 55% of them were straight in the rod cells ($n = 27$) while most of the stalled sheaths in the spheroplast cells were slightly curved (mean, 0.32 $\mu m^{-1} \pm 0.11$; $n = 10$) and shorter than average (mean, 3.04 $\mu m \pm 0.40$; $n = 10$). These results suggest that TagA is not required for the curved sheath to enter a stalling stage prior to contraction. In addition, and perhaps more importantly, we found that the curved stalling structures could resume growth (see Fig. S4C in the supplemental material), suggesting that the stalling might not be caused by an end cap that blocks growth.

T6SS is functional under curvy-sheath induction condition. A previous study examining the T6SS straight structures in spheroplast cells showed that the T6SS is functional after a relatively short period of antibiotic exposure (9). Here, we tested whether the curved T6SS structures that are induced by longer antibiotic exposure are functional. Because cell wall-deficient cells are prone to lysis releasing cytoplasmic proteins to the medium, we used a sensitive T6SS complement assay using the T6SS null *hcp1/2* and *vgrG2* mutants as reporters as previously described (9, 39). The reporter strains cannot assemble T6SS sheath/Hcp structure due to the lack of key structural components unless the missing components are provided through delivery by a donor cell. Indeed, we readily detected sheath formation in both reporter strains under the curvy-sheath induction conditions whereas none was detected when the donor was the T6SS null mutant (Fig. 4A) (see Fig. S5A and B in the supplemental material). More

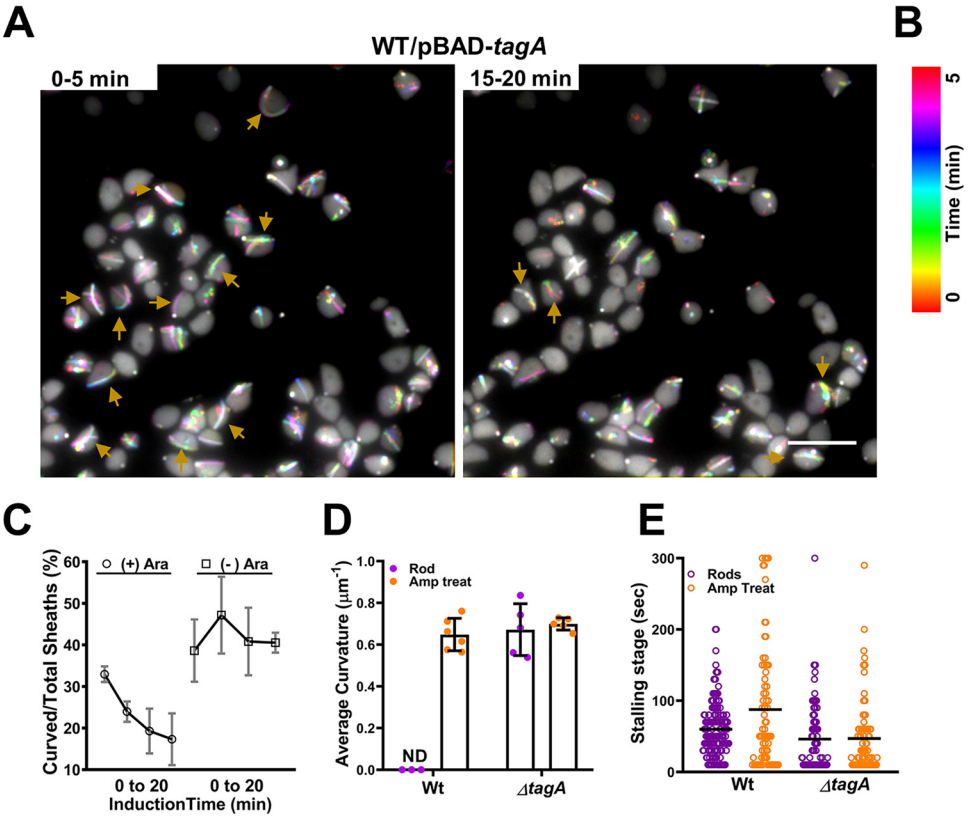

FIG 3 Reduction of curved T6SS sheaths by TagA. (A) Color-coded images show numbers of curved sheaths assembled between 0 to 5 min (left) and between 15 to 20 min (right) after induction of plasmid pBAD-*tagA* in the wild-type (WT) VipA-sfGFP strain with 0.05% L-arabinose. Curved sheaths are indicated by yellow arrows. Images show representative fields of view (FOV) of 30 by 30 μm acquired during recording of a 20-min time-lapse video with a 10-s frame rate. Full videos are provided as Movie S4. Scale bar, 5 μm. (B) Color code (spectrum) and time scale in minutes correspond to the images in panel A. (C) Graph showing trend lines of curved sheath percentages over total sheaths assembling after induction of plasmid pBAD-*tagA* in the WT VipA-sfGFP strain. Cells were induced with 0.05% L-arabinose [(+) Ara] or with PBS [(−) Ara] for 20 min. Sheaths were counted in four windows of time: 0 to 5, 5 to 10, 10 to 15, and 15 to 20 min after induction. Time-lapse videos were taken at a rate of 10 s per frame. Three biological replicates were performed under each set of conditions. A representative FOV is shown in panel A and in Movie S4. (D) Average curvature of sheaths assembled in either the WT or the *tagA* deletion strain (Δ*tagA*) in rods (purple circles) and spheroplasts (orange circles). Each data point represents an independent biological replicate. ND, not detected. (E) Stalling stage data (in seconds) represent the time frame of fully extended sheaths before contraction in the WT or Δ*tagA* strain in rod (purple) or spheroplast (orange) cells. Each data point represents a sheath. The median value is indicated by a black line.

sheaths were observed in the *hcp* mutant, while longer sheaths were observed in the *vgrG2* mutant (Fig. 4A and B), reflecting the fact that one VgrG trimer and a stack of Hcp hexameric rings are needed to assemble a functional extended sheath-Hcp structure. Although we cannot prevent substrate delivery by straight structures from spheroplasts, donor cells surrounding reporter recipient cells fired 20% more curved than straight T6SS structures (see Fig. S5D in the supplemental material).

The H1-T6SS in *Pseudomonas aeruginosa* PAO1 can respond to external T6SS attacks and thus can be used as a reporter for T6SS delivery as well (40). Indeed, under the curvy-sheath induction condition, significantly more T6SS activities in PAO1 were observed when PAO1 cells were neighboring wild-type *V. cholerae* than when they were surrounding the *hcp* mutant (Fig. 4C) (see Fig. S5C in the supplemental material).

Next, we tested whether the curved sheath could contract normally and be disassembled by the ATPase ClpV. The otherwise buried VipB N-terminal domain is exposed only after sheath contraction and is specifically recognized by the ClpV ATPase that disassembles the contracted sheath (23–26). The curved extended sheaths were not recognized by ClpV, but contraction quickly led to ClpV coating of the sheath, indicat-

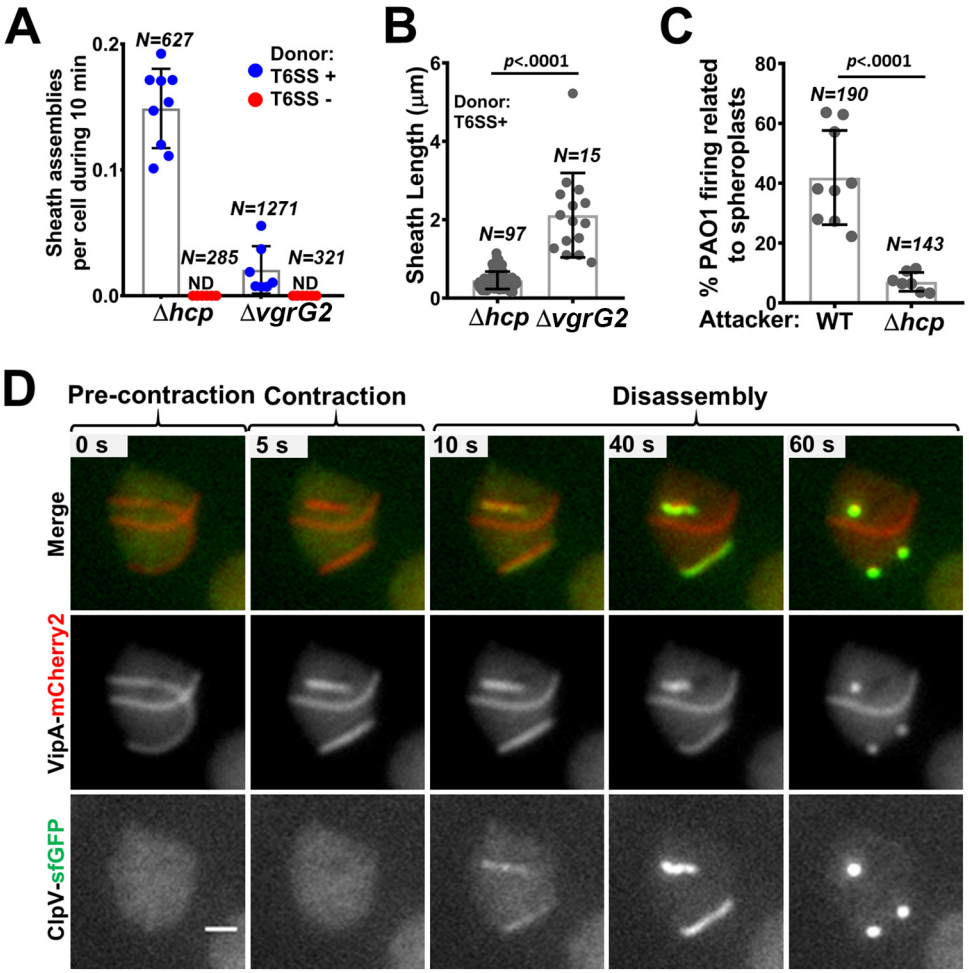

FIG 4 Functionality of curved T6SS sheaths. (A) Numbers of sheaths assembled in the VipA-sfGFP recipient strains (the Δ*hcp* strain and the Δ*vgrG2* strain) during 10 min of coincubation with either the WT VipA-mCherry2 strain (donor T6SS +) or the unlabeled Δ*vipB* strain (donor T6SS −) are shown. Recipient and donor cells were treated with ampicillin, mixed in a 3:1 (donor-to-recipient) ratio, and incubated on agarose pads for 3 h before imaging. Three videos from each of the three biological replicates were analyzed under each set of conditions. The number of cells counted (*N*) is indicated at the top. ND, not detected. Representative image sequences are shown in Fig. S5A and B in the supplemental material. (B) Sheath length was measured for each sheath formed in both recipient strains (the VipA-sfGFP-Δ*hcp* strain and the Δ*vgrG2* strain) coincubated with the T6SS-positive (T6SS$^+$) strain. The number of sheaths observed (*N*) is indicated at the top. (C) Percentage of foci assembled by *P. aeruginosa* PAO1-TssB-sfGFP surrounding either WT or Δ*hcp*-VipA-mCherry2 *V. cholerae* spheroplasts over the total number of foci observed during 20 min. Each data point represents a video from three biological replicates. Total numbers of foci observed (*N*) are indicated at the top. A representative example is included in Fig. S5C in the supplemental material. (D) Image sequence of doubly labeled VipA-mCherry2; ClpV-sfGFP cell shows curved sheath precontraction and contraction and subsequent disassembly by ClpV. The frames on the top row correspond to a merge of mCherry2 (red) and GFP (green) fluorescence channels. The middle and bottom rows show only VipA-mCherry2 and ClpV-sfGFP signals, respectively, in grayscale. The original video was a 5-min time-lapse video (5.5 s per frame). Additional examples are provided in Fig. S5E and Movie S5 in the supplemental material. Scale bar, 1 μm.

ing that the VipB N terminus was inaccessible in the curved extended sheath in the same manner as in the straight extended sheath (Fig. 4D) (see Fig. S5E and Movie S5 in the supplemental material). These results collectively suggest that at least some, if not all, curved sheath-tube structures are functional.

DISCUSSION

The bacterial cell wall is an essential structure supporting numerous physiological activities and is thus a major target for antimicrobial treatment. However, both Gram-positive and Gram-negative pathogens are able to enter under conditions of a cell wall-deficient state, which represents an important adaptation strategy (29). Loss of cell

wall presumably has a direct impact on the cellular organelles that are anchored by transenvelope complexes, including many responsible for translocating virulence factors. Here, we show that removal of cell wall induced striking conformational changes of the T6SS sheath/tube whereas such curvy deformation did not seem to affect functionality. Interestingly, membrane contact did not trigger contraction or prevent sheath/tube subunits from being recruited to the growing distal end of the T6SS structure in both spheroplast cells and rod cells lacking TagA. Formation of curvy T6SS structures in spheroplast cells likely results from insufficient accessibility of TagA due to degradation or dilution in spheroplasts. This conjecture is supported by the observations that curvy sheaths were found only at later but not earlier time points after ampicillin treatment and were inhibited by expression of TagA. These results demonstrate the multifaceted effects that cell wall deficiency might have on intracellular organelles.

There is a stalling/residence stage of T6SS prior to contraction in both the wild-type strain and the *tagA* mutant. These observations are consistent with previous findings in enteroaggregative *E. coli* (21). However, a substantial number of extended structures remain stable even in the *tagA* mutant, suggesting that other factors may contribute to stabilization in addition to the proposed TagA clamp (21, 41). More importantly, the stalled extended sheath/tube is not destined to contraction but is able to resume extension. These results and previous findings indicating that T6SS does not randomly contract when Hcp and sheath precursors are being recruited during extension (9, 39) collectively support a model in which the highly interactive affinity between sheath-tube subunits renders extension an energetically favorable reaction and contributes to stability.

The T6SS is mechanistically and evolutionarily related to other contractile needle-like cell-puncturing devices, including R-type pyocins (42, 43), *Photorhabdus* virulence cassettes (PVC) (44), *Serratia* antifeed prophage (45), and contractile phage tail (46, 47). The sheath is assembled into a high-energy extended state, and contraction completes almost instantly (less than 2 ms for T6SS) (9), which enables a powerful penetration to breach the target cell. Although several contractile phage tails have displayed some flexibility in imaging by electron microscopy (48–50), our results provide direct evidence in live cells for the flexibility and elasticity of the double tubular structure. The functional assays show that the T6SS is still functional under the curvy-needle induction conditions. Because it is technically infeasible to prevent straight structure formation under all conditions, it is plausible that the observed T6SS functions are attributable to both curvy and straight T6SS structures, but the possibility that straight structures represent the sole contributors is low.

Because the cell wall is a major antimicrobial drug target, the proper control of size/shape of an organelle in eukaryotic and prokaryotic cells is a fundamental biological issue (51, 52) and because the cell wall-deficient state is used for modeling primordial cellular activities (29), this study should be of broad interest to researchers in many disciplines, including drug development, theoretical biology, evolution, and bioengineering, as well as physics.

MATERIALS AND METHODS

Bacterial strains and growth conditions. The strains and plasmids used in this study are listed in Tables S1 and S2, respectively in the supplemental material. Cells were grown aerobically at 37°C in LB (1% [wt/vol] tryptone, 0.5% [wt/vol] yeast extract, 0.5% [wt/vol] NaCl). Antibiotics were used at the following concentrations: chloramphenicol at 25 μg/ml (for *E. coli*) and 2.5 μg/ml (for *V. cholerae*), kanamycin at 50 μg/ml, gentamicin at 20 μg/ml, streptomycin at 100 μg/ml, and irgasan at 25 μg/ml. Gene expression vectors and precisely designed knockout mutants were constructed as described previously (53). All constructs were verified by sequencing. All primers used in this study are provided in Table S3.

Induction of spheroplasts by ampicillin treatment. Overnight cultures were diluted 1:100 in 2 ml of fresh LB and grown aerobically at 37°C to an optical density at 600 nm (OD_{600}) of 0.6 to 0.8. Ampicillin was added to the cultures at 500 μg/ml, and the cultures were further incubated for 45 min. Cultures were centrifuged, and the resulting pellets were resuspended in 0.5× phosphate-buffered saline (PBS) buffer. Cells were spotted onto 1% agarose pads supplemented with diluted LB (1:5), PBS buffer (1:2), and ampicillin (10 μg/ml). Spotted microscope slides were incubated at 37°C and imaged at different time points.

***V. cholerae* Δ*mrcA* spheroplasts.** An overnight culture of the Δ*mrcA* strain was centrifuged, and the pellet was resuspended in fresh LB. After incubation at 37°C for 1 h, cells were concentrated to an OD_{600} of 20 and spotted onto 1% agarose–0.5× PBS pads supplemented with diluted LB (1:5). The spotted microscope slides were incubated at 37°C prior to imaging.

Cell lysis induction. *V. cholerae* VipA-N3–superfold green fluorescent protein (sfGFP) cells were grown to an OD_{600} of 0.6 to 0.8 and treated with 500 μg/ml ampicillin for 45 min. Cells were then collected and spotted onto an agarose pad under spheroplast induction conditions, as explained before. After incubation of the spotted microscopy slides at 37°C, the coverslip was carefully removed and a mixture of 1 μl of 80 μg/ml colistin, 0.1% Triton X, and 1 μl of 10 μg/ml DAPI (4′,6-diamidino-2-phenylindole) was deposited on top of the agarose pad. A new coverslip was added, and cell lysis was quickly monitored by time-lapse fluorescence microscopy at a rate of 10 s per frame until all observed cells were lysed (approximately 30 min).

Functionality assays under curvy structure conditions. For the T6SS interbacterial complementation assay, Δ*hcp1/2* VipA-sfGFP and Δ*vgrG2* VipA-sfGFP strains were used as recipient cells. The wild-type VipA-mCherry2 ($T6SS^+$) strain and the Δ*vipB* ($T6SS^-$) strain were used as donor strains. Both donor and recipient cells were treated similarly with 500 μg/ml of ampicillin, harvested, and then mixed to reach a 1:3 (recipient-to-donor) ratio for imaging. Sheath formation in the recipient strains was monitored using time-lapse fluorescence microscopy at a rate of 10 s per frame for 10 min.

For the *P. aeruginosa* PAO1 reporter assay, *V. cholerae* wild-type ($T6SS^+$) and Δ*hcp1/2* ($T6SS^-$) VipA-mCherry2 strains were grown to the exponential phase and treated with ampicillin. Cells were spotted onto 1% agarose–0.5× PBS pads supplemented with LB and ampicillin and incubated to induce formation of curvy sheaths. The glass coverslip was carefully removed, and exponentially growing PAO1 TssB-sfGFP rod cells were spotted on top of the *V. cholerae* containing-agarose pads. A new glass coverslip was added, and cells were immediately imaged every 10 s using time-lapse fluorescence microscopy.

Imaging of *tagA* deletion strains. For imaging *V. cholerae* rod cells, overnight cultures were subcultured in fresh LB (1:100) and grown to an OD_{600} of 0.8 to 1.0 in a shaker at 37°C. An aliquot of 200 μl was spun down and concentrated to an OD_{600} of 20 in 0.5× PBS buffer. Cells were then spotted onto a 1% agarose–0.5× PBS pad supplemented with diluted LB (1:5) and 0.01% L-arabinose when indicated. Images were taken for 5 min at a rate of 10 s per frame.

To assess if expression of *tagA* restores the curved sheath phenotype in spheroplasts, wild-type VipA-sfGFP cells carrying a pBAD-*tagA* plasmid were treated with 500 μg/ml of ampicillin as explained above and incubated under curved-sheath induction conditions. At that point, the coverslip was carefully removed and 1 μl of 0.05% L-arabinose mixed with PBS or PBS only was added on top of the *V. cholerae*-containing agarose pads. Cells were imaged immediately by time-lapse fluorescence microscopy for 20 min at a rate of 10 s per frame.

Bacterial killing assay. Overnight cultures of killer cells were diluted in LB (1:100) and grown to an OD_{600} of 0.8 to 1.0. To induce pBAD plasmid expression, 0.01% L-arabinose was added to the liquid media for 15 min. Cells were then harvested and mixed with *E. coli* MG1655 prey (grown overnight) at a 10:1 (killer-to-prey) ratio. The mix was spotted onto a LB–0.01% L-arabinose plate and incubated for 3 h at 37°C. Cells were then collected and resuspended in 400 μl of LB, and 10-fold serial dilutions were plated onto LB agar with 20 μg/ml gentamicin to assess the survival of the *E. coli* MG1655 prey. All killing assays were performed in triplicate. The mean $\log_{10}$ CFU counts representing prey survival in three or four biological replicates are plotted in bar graphs, and standard deviation (SD) is indicated with error bars.

Imaging of ClpV-labeled strains. To image ClpV-mediated disassembly, *V. cholerae* VipA-mCherry2 ClpV-sfGFP cells were treated as explained before for formation of curved sheaths and visualized after incubation at 37°C on the agarose pad. Cells were imaged by time-lapse fluorescence microscopy for 8 min at a rate of either 5.5 or 10 s per frame.

Image acquisition. All images were acquired by the use of a Nikon Ti-E inverted microscope with a Perfect Focus System (PFS) and a CFI plan apochromat lambda 100× oil lens objective. Different fluorescence signals were filtered and excited using an Intensilight C-HGFIE illuminator (Nikon) with ET-GFP (Chroma 49002) and ET-mCherry2 (Chroma 49008) filter sets. Images were recorded by the use of an Andor Clara camera (DR 328G-C01-SIL) (pixel size, 60 nm) and NIS-Elements AR 4.40 software.

Image analysis. Fiji was used for all image analysis (54). To correct for photobleaching, the fluorescence intensity of the acquired time-lapse videos was normalized to the same mean intensity for each image in a time series as described previously (40). The plug-in "Temporal-Color Code" for Fiji was used to visualize the polymerization trajectory of the curved sheath in Fig. 1B and to evaluate the effect of TagA expression on wild-type VipA-sfGFP spheroplasts (Fig. 3A). Relative levels of brightness and contrast of the images were adjusted equally among data sets. The area of the cells was measured using the freehand selection tool in Fiji. Lengths of straight and curved sheaths were measured using straight and freehand line tools, respectively. The curvature analysis was performed using the plug-in "Kappa" for Fiji. The curvature is defined as the reciprocal of the radius (r^{-1}). For sheaths with negative curvature points, the absolute values of curvature were used to build graphs and calculate mean values. Five points were used to define each curved sheath, and the scale was set to 0.064 μm/pixel. We measured 120 fully extended curved sheaths in wild-type spheroplasts (80 from ampicillin-treated spheroplasts and 40 from Δ*mrcA* spheroplasts) and 100 curved sheaths in the *tagA* deletion strain (50 for rod cells and 50 for spheroplasts). The "KymoResliceWide" plug-in for Fiji was used to generate the kymographs shown in Fig. S4C in the supplemental material. The freehand line tool was used to define the sheath area to generate the kymographs. Stalling-stage data, corresponding to the number of frames (in seconds) of a fully extended sheath before contraction, were manually quantified under each set of conditions. Only

sheaths that extended and contracted in 5-min time-lapse videos at a rate of 10 s per frame were considered.

Quantification and statistical analysis. The unpaired two-tailed *t* test was performed using GraphPad Prism version 8.0.0. Numbers of cells analyzed as well as the statistical significance of each comparison are indicated in the figures and figure legends. All experiments were performed with at least three biological replicates. Unless indicated differently, values are expressed as means ± SD.

SUPPLEMENTAL MATERIAL

Supplemental material is available online only.

SUPPLEMENTAL FILE 1, PDF file, 1.5 MB.

SUPPLEMENTAL FILE 2, MP4 file, 15.3 MB.

SUPPLEMENTAL FILE 3, MP4 file, 4.4 MB.

SUPPLEMENTAL FILE 4, MP4 file, 15.6 MB.

SUPPLEMENTAL FILE 5, MP4 file, 5.3 MB.

SUPPLEMENTAL FILE 6, MP4 file, 17.3 MB.

ACKNOWLEDGMENTS

This work was supported by grants from the Canadian Institutes of Health Research and the Natural Sciences and Engineering Research Council (NSERC) to T.G.D. T.G.D. is supported by a Canada Research Chair award. We thank members of the Dong laboratory for providing reagents, for general support, and for critical reading of the manuscript.

T.G.D. conceived the project. M.S.S., X.L., and T.G.D. designed the experiments. M.S.S., X.L., M.W., and S.H. performed the experiments. M.S.S. and T.G.D. prepared the manuscript.

We declare that we have no competing interests.

REFERENCES

1. Stubbendieck RM, Straight PD. 2016. Multifaceted Interfaces of bacterial competition. J Bacteriol 198:2145–2155. https://doi.org/10.1128/JB.00275-16.
2. Czárán TL, Hoekstra RF, Pagie L. 2002. Chemical warfare between microbes promotes biodiversity. Proc Natl Acad Sci U S A 99:786–790. https://doi.org/10.1073/pnas.012399899.
3. Anderson MS, Garcia EC, Cotter PA. 2014. Kind discrimination and competitive exclusion mediated by contact-dependent growth inhibition systems shape biofilm community structure. PLoS Pathog 10:e1004076. https://doi.org/10.1371/journal.ppat.1004076.
4. Wong MJQ, Liang X, Smart M, Tang L, Moore R, Ingalls B, Dong TG. 2016. Microbial herd protection mediated by antagonistic interaction in polymicrobial communities. Appl Environ Microbiol 82:6881–6888. https://doi.org/10.1128/AEM.02210-16.
5. Pukatzki S, Ma AT, Sturtevant D, Krastins B, Sarracino D, Nelson WC, Heidelberg JF, Mekalanos JJ. 2006. Identification of a conserved bacterial protein secretion system in *Vibrio cholerae* using the Dictyostelium host model system. Proc Natl Acad Sci U S A 103:1528–1533. https://doi.org/10.1073/pnas.0510322103.
6. Mougous JD, Cuff ME, Raunser S, Shen A, Zhou M, Gifford CA, Goodman AL, Joachimiak G, Ordoñez CL, Lory S, Walz T, Joachimiak A, Mekalanos JJ. 2006. A virulence locus of *Pseudomonas aeruginosa* encodes a protein secretion apparatus. Science 312:1526–1530. https://doi.org/10.1126/science.1128393.
7. Ho BT, Dong TG, Mekalanos JJ. 2014. A view to a kill: the bacterial type VI secretion system. Cell Host Microbe 15:9–21. https://doi.org/10.1016/j.chom.2013.11.008.
8. Basler M, Pilhofer M, Henderson GP, Jensen GJ, Mekalanos JJ. 2012. Type VI secretion requires a dynamic contractile phage tail-like structure. Nature 483:182–186. https://doi.org/10.1038/nature10846.
9. Vettiger A, Winter J, Lin L, Basler M. 2017. The type VI secretion system sheath assembles at the end distal from the membrane anchor. Nat Commun 8:16088–16089. https://doi.org/10.1038/ncomms16088.
10. Brunet YR, Zoued A, Boyer F, Douzi B, Cascales E. 2015. The type VI secretion TssEFGK-VgrG phage-like baseplate is recruited to the TssJLM membrane complex via multiple contacts and serves as assembly platform for tail tube/sheath polymerization. PLoS Genet 11:e1005545. https://doi.org/10.1371/journal.pgen.1005545.
11. Durand E, Nguyen VS, Zoued A, Logger L, Péhau-Arnaudet G, Aschtgen M-S, Spinelli S, Desmyter A, Bardiaux B, Dujeancourt A, Roussel A, Cambillau C, Cascales E, Fronzes R. 2015. Biogenesis and structure of a type VI secretion membrane core complex. Nature 523:555–560. https://doi.org/10.1038/nature14667.
12. Wang J, Brackmann M, Castaño-Díez D, Kudryashev M, Goldie KN, Maier T, Stahlberg H, Basler M. 2017. Cryo-EM structure of the extended type VI secretion system sheath-tube complex. Nat Microbiol 2:1507–1512. https://doi.org/10.1038/s41564-017-0020-7.
13. Kudryashev M, Wang RY, Brackmann M, Scherer S, Maier T, Baker D, DiMaio F, Stahlberg H, Egelman EH, Basler M. 2015. Structure of the type VI secretion system contractile sheath. Cell 160:952–962. https://doi.org/10.1016/j.cell.2015.01.037.
14. Brackmann M, Nazarov S, Wang J, Basler M. 12 June 2017, posting date. Using force to punch holes: mechanics of contractile nanomachines. Trends Cell Biol https://doi.org/10.1016/j.tcb.2017.05.003.
15. Shneider MM, Buth SA, Ho BT, Basler M, Mekalanos JJ, Leiman PG. 2013. PAAR-repeat proteins sharpen and diversify the type VI secretion system spike. Nature 500:350–353. https://doi.org/10.1038/nature12453.
16. Pukatzki S, Ma AT, Revel AT, Sturtevant D, Mekalanos JJ. 2007. Type VI secretion system translocates a phage tail spike-like protein into target cells where it cross-links actin. Proc Natl Acad Sci U S A 104:15508–15513. https://doi.org/10.1073/pnas.0706532104.
17. Dong TG, Ho BT, Yoder-Himes DR, Mekalanos JJ. 2013. Identification of T6SS-dependent effector and immunity proteins by Tn-seq in *Vibrio cholerae*. Proc Natl Acad Sci U S A 110:2623–2628. https://doi.org/10.1073/pnas.1222783110.
18. Burkinshaw BJ, Liang X, Wong M, Le ANH, Lam L, Dong TG. 2018. A type VI secretion system effector delivery mechanism dependent on PAAR and a chaperone–co-chaperone complex. Nat Microbiol 3:632–640. https://doi.org/10.1038/s41564-018-0144-4.
19. Planamente S, Salih O, Manoli E, Albesa-Jové D, Freemont PS, Filloux A. 2016. TssA forms a gp6-like ring attached to the type VI secretion sheath. EMBO J 35:1613–1627. https://doi.org/10.15252/embj.201694024.
20. Zoued A, Durand E, Brunet YR, Spinelli S, Douzi B, Guzzo M, Flaugnatti N, Legrand P, Journet L, Fronzes R, Mignot T, Cambillau C, Cascales E. 2016. Priming and polymerization of a bacterial contractile tail structure. Nature 531:59–63. https://doi.org/10.1038/nature17182.

21. Santin YG, Doan T, Lebrun R, Espinosa L, Journet L, Cascales E. 2018. In vivo TssA proximity labelling during type VI secretion biogenesis reveals TagA as a protein that stops and holds the sheath. Nat Microbiol 3:1304–1313. https://doi.org/10.1038/s41564-018-0234-3.
22. Taylor N, Prokhorov NS, Guerrero-Ferreira RC, Shneider MM, Browning C, Goldie KN, Stahlberg H, Leiman PG. 2016. Structure of the T4 baseplate and its function in triggering sheath contraction. Nature 533:346–352. https://doi.org/10.1038/nature17971.
23. Bönemann G, Pietrosiuk A, Diemand A, Zentgraf H, Mogk A. 2009. Remodelling of VipA/VipB tubules by ClpV-mediated threading is crucial for type VI protein secretion. EMBO J 28:315–325. https://doi.org/10.1038/emboj.2008.269.
24. Kapitein N, Bönemann G, Pietrosiuk A, Seyffer F, Hausser I, Locker JK, Mogk A. 2013. ClpV recycles VipA/VipB tubules and prevents non-productive tubule formation to ensure efficient type VI protein secretion. Mol Microbiol 87:1013–1028. https://doi.org/10.1111/mmi.12147.
25. Basler M, Mekalanos JJ. 2012. Type 6 secretion dynamics within and between bacterial cells. Science 337:815–815. https://doi.org/10.1126/science.1222901.
26. Pietrosiuk A, Lenherr ED, Falk S, Bönemann G, Kopp J, Zentgraf H, Sinning I, Mogk A. 2011. Molecular basis for the unique role of the AAA^+ chaperone ClpV in type VI protein secretion. J Biol Chem 286:30010–30021. https://doi.org/10.1074/jbc.M111.253377.
27. Dong TG, Mekalanos JJ. 2012. Characterization of the RpoN regulon reveals differential regulation of T6SS and new flagellar operons in *Vibrio cholerae* O37 strain V52. Nucleic Acids Res 40:7766–7775. https://doi.org/10.1093/nar/gks567.
28. Kawai Y, Mickiewicz K, Errington J. 2018. Lysozyme counteracts β-lactam antibiotics by promoting the emergence of L-form bacteria. Cell 172:1038–1049.e10. https://doi.org/10.1016/j.cell.2018.01.021.
29. Errington J, Mickiewicz K, Kawai Y, Wu LJ. 2016. L-form bacteria, chronic diseases and the origins of life. Philos Trans R Soc Lond B Biol Sci 371:20150494. https://doi.org/10.1098/rstb.2015.0494.
30. Domingue GJ, Woody HB. 1997. Bacterial persistence and expression of disease. Clin Microbiol Rev 10:320–344. https://doi.org/10.1128/CMR.10.2.320.
31. Mercier R, Kawai Y, Errington J. 2013. Excess membrane synthesis drives a primitive mode of cell proliferation. Cell 152:997–1007. https://doi.org/10.1016/j.cell.2013.01.043.
32. Kawai Y, Mercier R, Wu LJ, Domínguez-Cuevas P, Oshima T, Errington J. 2015. Cell growth of wall-free L-form bacteria is limited by oxidative damage. Curr Biol 25:1613–1618. https://doi.org/10.1016/j.cub.2015.04.031.
33. Studer P, Staubli T, Wieser N, Wolf P, Schuppler M, Loessner MJ. 2016. Proliferation of *Listeria monocytogenes* L-form cells by formation of internal and external vesicles. Nat Commun 7:13631. https://doi.org/10.1038/ncomms13631.
34. Dörr T, Lam H, Alvarez L, Cava F, Davis BM, Waldor MK. 2014. A novel peptidoglycan binding protein crucial for PBP1A-mediated cell wall biogenesis in *Vibrio cholerae*. PLoS Genet 10:e1004433. https://doi.org/10.1371/journal.pgen.1004433.
35. Dörr T, Möll A, Chao MC, Cava F, Lam H, Davis BM, Waldor MK. 2014. Differential requirement for PBP1a and PBP1b in in vivo and in vitro fitness of *Vibrio cholerae*. Infect Immun 82:2115–2124. https://doi.org/10.1128/IAI.00012-14.
36. Basler M. 2015. Type VI secretion system: secretion by a contractile nanomachine. Philos Trans R Soc Lond B Biol Sci 370:20150021. https://doi.org/10.1098/rstb.2015.0021.
37. Taylor NMI, van Raaij MJ, Leiman PG. 2018. Contractile injection systems of bacteriophages and related systems. Mol Microbiol 108:6–15. https://doi.org/10.1111/mmi.13921.
38. Brackmann M, Wang J, Basler M. 2017. Type VI secretion system sheath inter-subunit interactions modulate its contraction. EMBO Rep https://doi.org/10.15252/embr.201744416.
39. Vettiger A, Basler M. 2016. Type VI secretion system substrates are transferred and reused among sister cells. Cell 167:99–110.e12. https://doi.org/10.1016/j.cell.2016.08.023.
40. Basler M, Ho BT, Mekalanos JJ. 2013. Tit-for-tat: type VI secretion system counterattack during bacterial cell-cell interactions. Cell 152:884–894. https://doi.org/10.1016/j.cell.2013.01.042.
41. Francetic O. 2018. Tagging the type VI secretion system. Nat Microbiol 3:1190–1191. https://doi.org/10.1038/s41564-018-0277-5.
42. Leiman PG, Shneider MM. 2012. Contractile tail machines of bacteriophages. Adv Exp Med Biol 726:93–114. https://doi.org/10.1007/978-1-4614-0980-9_5.
43. Ge P, Scholl D, Leiman PG, Yu X, Miller JF, Zhou ZH. 2015. Atomic structures of a bactericidal contractile nanotube in its pre- and postcontraction states. Nat Struct Mol Biol 22:377–382. https://doi.org/10.1038/nsmb.2995.
44. Yang G, Dowling AJ, Gerike U, Ffrench-Constant RH, Waterfield NR. 2006. Photorhabdus virulence cassettes confer injectable insecticidal activity against the wax moth. J Bacteriol 188:2254–2261. https://doi.org/10.1128/JB.188.6.2254-2261.2006.
45. Heymann JB, Bartho JD, Rybakova D, Venugopal HP, Winkler DC, Sen A, Hurst MRH, Mitra AK. 2013. Three-dimensional structure of the toxin-delivery particle antifeeding prophage of *Serratia entomophila*. J Biol Chem 288:25276–25284. https://doi.org/10.1074/jbc.M113.456145.
46. Rossmann MG, Mesyanzhinov VV, Arisaka F, Leiman PG. 2004. The bacteriophage T4 DNA injection machine. Curr Opin Struct Biol 14:171–180. https://doi.org/10.1016/j.sbi.2004.02.001.
47. Leiman PG, Basler M, Ramagopal UA, Bonanno JB, Sauder JM, Pukatzki S, Burley SK, Almo SC, Mekalanos JJ. 2009. Type VI secretion apparatus and phage tail-associated protein complexes share a common evolutionary origin. Proc Natl Acad Sci U S A 106:4154–4159. https://doi.org/10.1073/pnas.0813360106.
48. Klumpp J, Dorscht J, Lurz R, Bielmann R, Wieland M, Zimmer M, Calendar R, Loessner MJ. 2008. The terminally redundant, nonpermuted genome of Listeria bacteriophage A511: a model for the SPO1-like myoviruses of Gram-positive bacteria. J Bacteriol 190:5753–5765. https://doi.org/10.1128/JB.00461-08.
49. Chibani-Chennoufi S, Dillmann M-L, Marvin-Guy L, Rami-Shojaei S, Brüssow H. 2004. *Lactobacillus plantarum* bacteriophage LP65: a new member of the SPO1-like genus of the family Myoviridae. J Bacteriol 186:7069–7083. https://doi.org/10.1128/JB.186.21.7069-7083.2004.
50. Nováček J, Šiborová M, Benešík M, Pantůček R, Doškař J, Plevka P. 2016. Structure and genome release of Twort-like Myoviridae phage with a double-layered baseplate. Proc Natl Acad Sci U S A 113:9351–9356. https://doi.org/10.1073/pnas.1605883113.
51. Marshall WF. 2015. How cells measure length on subcellular scales. Trends Cell Biol 25:760–768. https://doi.org/10.1016/j.tcb.2015.08.008.
52. Chan Y-HM, Marshall WF. 2012. How cells know the size of their organelles. Science 337:1186. https://doi.org/10.1126/science.1223539.
53. Miller VL, Mekalanos JJ. 1988. A novel suicide vector and its use in construction of insertion mutations: osmoregulation of outer membrane proteins and virulence determinants in *Vibrio cholerae* requires toxR. J Bacteriol 170:2575–2583. https://doi.org/10.1128/jb.170.6.2575-2583.1988.
54. Schindelin J, Arganda-Carreras I, Frise E, Kaynig V, Longair M, Pietzsch T, Preibisch S, Rueden C, Saalfeld S, Schmid B, Tinevez J-Y, White DJ, Hartenstein V, Eliceiri K, Tomancak P, Cardona A. 2012. Fiji: an open-source platform for biological-image analysis. Nat Methods 9:676–682. https://doi.org/10.1038/nmeth.2019.